Evidence for superconductivity at $T_c = 12$ K in oxygen-deficient $MoO_{2-\delta}$ and properties of molybdenum arsenide and oxide binaries

D. Parker,[1] J. C. Idrobo,[2] C. Cantoni,[1] and A. S. Sefat[1]

[1]*Materials Science & Technology Division, Oak Ridge National Laboratory, Oak Ridge, Tennessee 37831, USA*

[2]*Center for Nanophase Materials Science Division, Oak Ridge National Laboratory, Oak Ridge, Tennessee 37831, USA*

(Received 8 April 2014; revised manuscript received 22 July 2014; published 7 August 2014)

We find signatures of superconductivity at $T_c = 12$ K in a molybdenum arsenide sample containing ~4% of $MoO_{2-\delta}$ impurity by weight. Below is a report on the electronic structure calculations, structures analyses, and thermodynamic and transport properties on Mo_2As_3, Mo_5As_4, and MoO_2, in order to uncover the reasons for superconductivity for the sample that contains a mixture of these phases. The experimental and theoretical evidence suggest that superconductivity in the $MoO_{2-\delta}$ phase is likely and may be caused by nesting-type fluctuations.

DOI: 10.1103/PhysRevB.90.054505 PACS number(s): 74.20.Pq, 74.70.Xa, 74.25.Bt

I. INTRODUCTION

The families of iron-based superconductors (FeSC), such as those based on LaFeAsO, $BaFe_2As_2$, LiFeAs, and $Sr_4V_2O_6Fe_2As_2$, share common structural building blocks of iron arsenides (FeAs) [1]. The thermodynamic and transport properties of numerous transition-metal *T*As binaries found VAs, CrAs and CoAs (3*d*), and RuAs (4*d*) as proxy compositions for likely superconductivity [2], while superconductivity was reported in 25% Rh-doped RuAs [3]. This is a report on the filamentary superconductivity in $MoO_{2-\delta}$ at $T_c \approx 12$ K detected in a batch that is a mixture of Mo_2As_3, Mo_5As_4, and MoO_2 crystalline phases. In addition to reporting on this batch, we present calculations, thermodynamic and transport properties, and also local structures of pure stoichiometric Mo_2As_3, Mo_5As_4, and MoO_2 (4*d*) binary phases.

No superconductivity has been observed in any of the binaries of Mo_2As_3, Mo_5As_4, or MoO_2. For Mo_2As_3 and MoO_2, the structures are made of networks of Mo-centered octahedra, while they are square planar and square pyramidal for Mo_5As_4 (Fig. 1). Mo_2As_3 crystallizes in monoclinic lattice ($C2/m$ space group) [4] and is diamagnetic [5]. Mo_5As_4 has tetragonal lattice ($I4/m$) [6] and is reported to change from a diamagnetic to a paramagnetic state at ~250 K [5]. MoO_2 crystallizes in a monoclinic lattice ($P2_1/c$) [7], and is Pauli paramagnet metal with $\rho \approx 10^{-4}$ ohm cm at 300 K and 10^{-6} ohm cm at 4 K [8]. Superconductivity is observed in bcc elemental Mo with $T_c = 0.9$ K, and the trigonal Chevrel ternaries of $A_xMo_6X_8$ (A = any element; X = Se, Se, or Te) reaching $T_c \approx 15$ K [9]. For a potassium-doped oxygen-deficient $K_xMoO_{2-\delta}$ ternary, $x = 0.05$ and $\delta = 0.37$ (monoclinic MoO_2 structure, interstitial K) signature of superconductivity was evident at $T_c = 6.5$ K (at 200 Oe) in magnetic susceptibility with ~4% superconducting volume fraction [10]. Another report found a diamagnetic transition at $T_c = 9.5$ K ($x = 0.05$) with the magnetic-field dependence of resistive transition [11]. Here we report filamentary superconductivity at $T_c = 12$ K in a sample that contains ~4% of oxygen deficient molybdenum oxide by weight, and we believe that this phase is related to that of $K_xMoO_{2-\delta}$, and so the monoclinic MoO_2 structure is prone to superconductivity.

Below is a report on the density functional theory (DFT) electronic structure calculations, structures analyses, and thermodynamic and transport properties on stoichiometric Mo_2As_3, Mo_5As_4, and MoO_2, in order to uncover the reasons for superconductivity for a sample that contains a mixture of these phases. Experimental results include temperature-dependent electrical transport and heat capacity, and temperature- and field-dependent magnetization data.

II. EXPERIMENTAL PROCEDURE

Polycrystalline samples of Mo_2As_3 and Mo_5As_4 were prepared by following several solid-state heating reactions, strictly in evacuated silica ampoules, and using the appropriate stoichiometric molar amounts of 2:3 and 5:4, respectively, of reduced Mo:As elemental ratios. For the synthesis of these binary materials, and because of the volatility of arsenic, slow heating was done. First, elemental powders were heated to 350 °C (50 °C/h; hold 5 h), to 600 °C (30 °C/h; hold 20 h), then to 650 °C (20 °C/h; hold 40 h), followed by furnace shut-down. The resulting mixtures were pelletized, and annealed a second time to 875 °C (200 °C/h; hold 45 h), followed by furnace shut-down. For phase pure Mo_2As_3 product, the final repelletizing and annealing procedure was performed at 1080 °C (200 °C; hold 80 h). For phase pure Mo_5As_4, final reaction was at done at 975 °C (200 °C; hold 50 h). In the various attempts to obtain phase-pure products, a batch resulted in mixtures of molybdenum arsenide and oxide (Mo_2As_3, Mo_5As_4, and MoO_2) crystalline phases, according to x-ray powder diffraction results. This batch, which we call $Mo_xAs_yO_z$ for the rest of this report, gave evidence for superconductivity, serendipitously.

The phase purity and structural identification were made via powder x-ray diffraction using PANalytical X'pert PRO MPD. Lattice constants of all samples were determined at room temperature from LeBail refinements using X'Pert HighScore Plus (2.2e version). dc magnetization was measured as a function of temperature using a Quantum Design magnetic property measurement system (MPMS). For the typical temperature sweep experiment, the sample was zero-field cooled (zfc) to 1.8 K and data were collected by warming from 2 K in an applied field. The sample was then field cooled (fc) in the applied field, and the measurement was repeated from 2 K. The temperature dependence of dc electrical resistance and

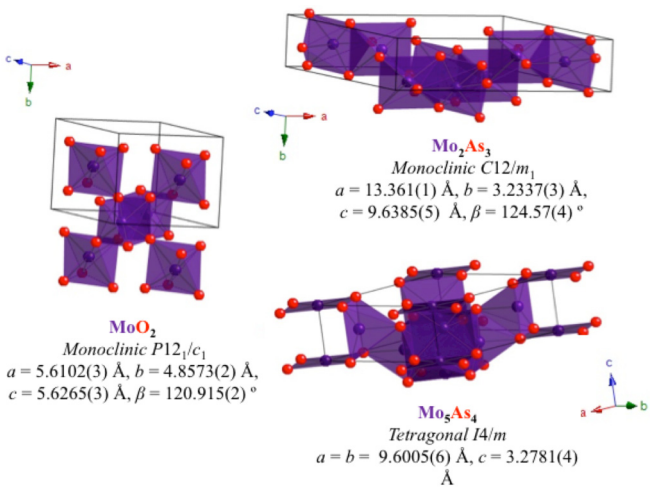

FIG. 1. (Color online) The crystal structures of Mo-based binaries of Mo_2As_3, Mo_5As_4, and MoO_2. The space group and literature's unit-cell parameters are listed [4,6,7].

heat capacity were measured using a Quantum Design physical property measurement system (PPMS). Electrical contacts were placed on samples in standard four-probe geometry by using Pt wires and Dupont silver paste. The local atomic arrangements of the samples were studied using an aberration-corrected scanning tunneling electron microscopy, STEM Nion UltraSTEM 100™, which has a cold field-emission electron source and that can correct third and fifth-order aberrations [12]. The microscope was operated at 100 kV acceleration voltage, using a 30 mrad semiconvergence angle. High-angle annular dark-field (HAADF) Z-contrast images were collected from ~86 to 200 mrad half-angle range.

III. EXPERIMENTAL RESULTS AND DISCUSSIONS

Powder x-ray diffraction data show that Mo_2As_3 and Mo_5As_4 phases can be made phase pure. Lattice parameters were determined from full-pattern LeBail refinements using X'Pert HighScore; these values compare well with those listed from literature in Fig. 1: for Mo_2As_3, $a = 13.3684(1)$ Å, $b = 3.2347(3)$ Å, $c = 9.642(1)$ Å, and $\beta = 124.593(1)$º; for Mo_5As_4, $a = 9.5957(1)$ Å and $c = 3.2273(1)$ Å. For the $Mo_xAs_yO_z$ batch, the powder diffraction data were well refined using three crystalline phases of 70.0% Mo_2As_3 [refined values of $a = 13.3624(3)$ Å, $b = 3.2347(1)$ Å, $c = 9.63495(2)$ Å, and $\beta = 124.563(1)$º], 26.1% Mo_5As_4 [$a = 9.5966(2)$ Å and $c = 3.2786(1)$ Å], and 3.8% amount of MoO_2 phase [$a = 5.5397(7)$ Å, $b = 4.8566(7)$ Å, $c = 5.6260(8)$ Å, and $\beta = 119.70(1)$º] with a unit-cell volume that is ~0.4% smaller than that of literatures, so slight oxygen deficiency may be expected. Thus our findings agree with those of Ref. [10], where no evidence for superconductivity was found in virtually stoichiometric MoO_2.

Figure 2 shows the transmission electron microscopy (TEM) images of atomic arrangements of Mo_2As_3 and Mo_5As_4 structures along different crystallographic orientations. For $Mo_xAs_yO_z$, the sample was composed by particles of 1–2 μm in size and grains of a few tenths of a micron large; selective area diffraction showed the presence of both Mo_2As_3

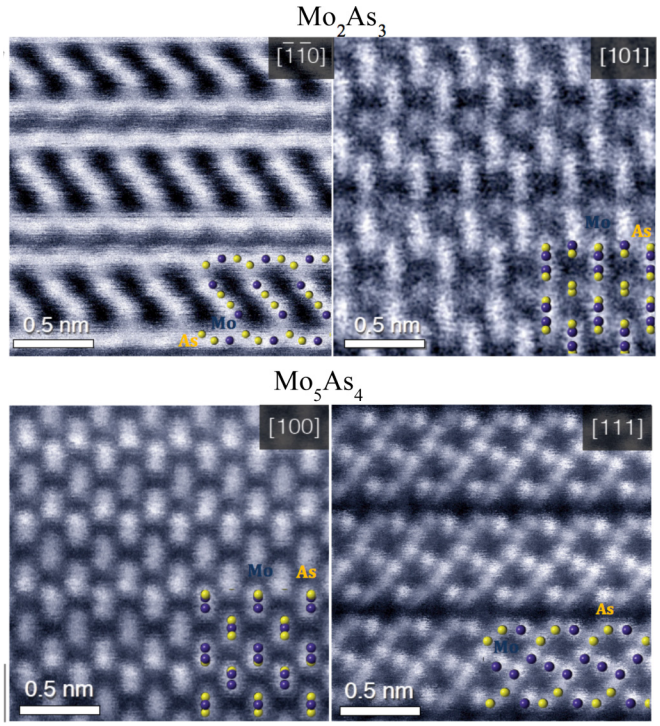

FIG. 2. (Color online) Z-contrast STEM images showing the atomic arrangements of structures of Mo_2As_3 and Mo_5As_4. Purple and yellow circles schematically show the atomic positions of the Mo and As, respectively.

and Mo_5As_4 particles. Energy dispersive spectroscopy (EDX), performed within the electron transmission microscope in scanning mode, confirmed the existence of an oxygen containing phase embedded within a particle of composition Mo_5As_4. Figure 3(a) shows a low resolution Z-contrast STEM image of the Mo_5As_4 particle and the region chosen for elemental EDX mapping. Figures 3(b)–3(d) show the EDX maps of this region for O K, Mo K, and As K edges, respectively, and indicate the presence of an oxide phase corresponding to the darker contrast region (lower Z) in the STEM image. The EDX spectra for the Mo_5As_4 phase and the oxygen-containing phase are shown in Figs. 3(e) and 3(f). No nitrogen signal was observed in any of the particles analyzed by EDX.

Figure 4 shows the temperature dependence of resistivity $\rho(T)$ and heat capacity $C(T)$. All samples are metallic, with resistivity decreasing with lowering temperature [Fig. 4(a)]. Upon the application of 8 Tesla, no shift in signal were noted for Mo_2As_3 or Mo_5As_4. For $Mo_xAs_yO_z$, there is a further downturn in resistivity below ~15 K [inset of Fig. 4(a)] and 8 Tesla seems to saturate the resistivity to ~0.07 mOhm cm at 2 K. $C(T)$ data are featureless for all three samples [Fig. 4(b)]. The plot of C/T versus T^2 is linear for Mo_2As_3 and Mo_5As_4 below ~10 K [Fig. 4(b), inset], while it is linear only below ~6 K for $Mo_xAs_yO_z$. Both Mo_2As_3 and $Mo_xAs_yO_z$ yield a residual Sommerfeld coefficient of $\gamma_0 \approx 7.2$ mJ K^{-2} mol^{-1}, while Mo_5As_4 gives $\gamma_0 \approx 13.4$ mJ K^{-2} mol^{-1}. The theoretically calculated values (from the first-principles calculations) for these specific heat coefficients, respectively, are 3.35 and 9.58 mJ/K^{-2} mol^{-1}, so that the experimental values for Mo_2As_3 and Mo_5As_4 are enhanced from the DFT values by

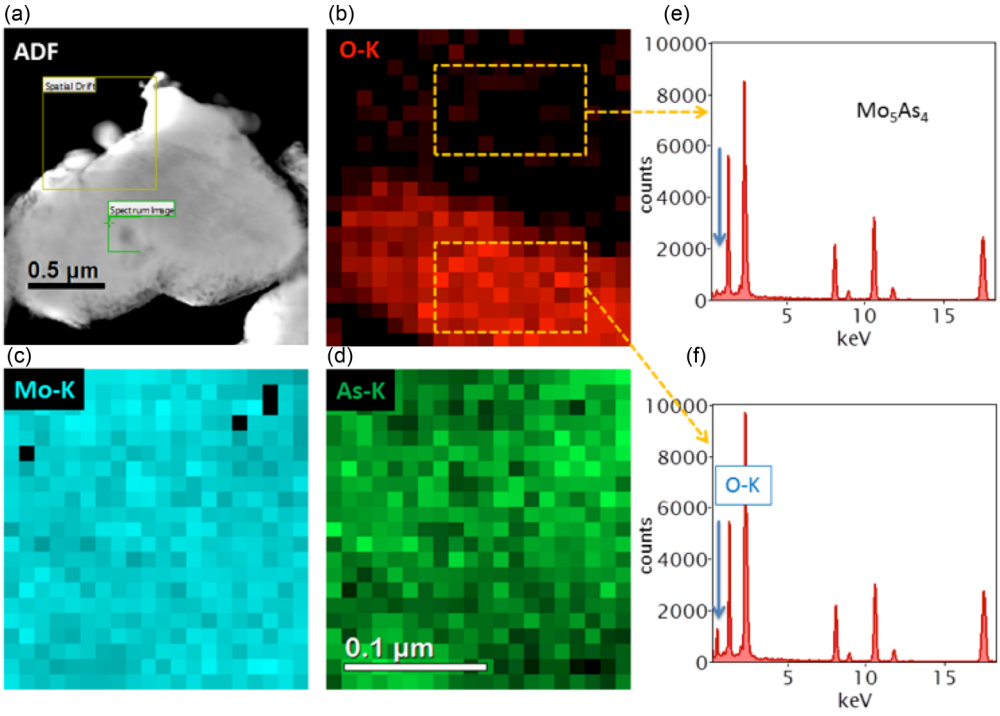

FIG. 3. (Color online) For a Mo-oxide phase embedded within particle of $Mo_xAs_yO_z$ batch. (a) Z-contrast image. (b) EDX O K map acquired within the green box drawn in (a), showing an oxygen-containing region within the grain. (c) and (d) Corresponding Mo K and As K edges maps for the same region. (e) EDX spectrum collected away from the Mo-O precipitate [upper rectangle in (b)], revealing a matrix composition of Mo_5As_4. (f) EDX spectrum collected from the oxygen-containing region [lower rectangle in (b)] with the arrow indicating the O K-edge position in both spectra.

factors of 2.15 and 1.40, respectively. While it is conceivable that such an enhancement could originate from an impurity component, this appears unlikely in view of the rather large residual resistivity ratios and the lack of crystalline impurity phases. It is more likely that these increases relative to the theoretical values reflect (at least to a degree) electron-phonon coupling, which generally increases specific heat coefficients relative to "bare" calculated values. The enhancement in this case would suggest electron-phonon coupling constants λ of 1.15 and 0.4 for Mo_2As_3 and Mo_5As_4, respectively. While the latter value is in the 0.32–0.43 range estimated for metallic (and superconducting) Mo [13], the former value is far outside this range, and hints at possible correlation effects in Mo_2As_3, though the nature of such correlations, if present, remains mysterious.

Figure 5 shows the temperature dependence of magnetic susceptibility $\chi(T)$. Mo_2As_3 shows diamagnetic behavior at $\sim 7 \times 10^{-5}$ emu mol^{-1} Oe^{-1}. $Mo_xAs_yO_z$ also gives diamagnetic behavior with similar temperature dependence, with the addition of a sharp downturn below 12 K. For calculating $\chi(T)$ for $Mo_xAs_yO_z$, the correct molar amounts of the crystalline phases, as detected above, in diffraction, were

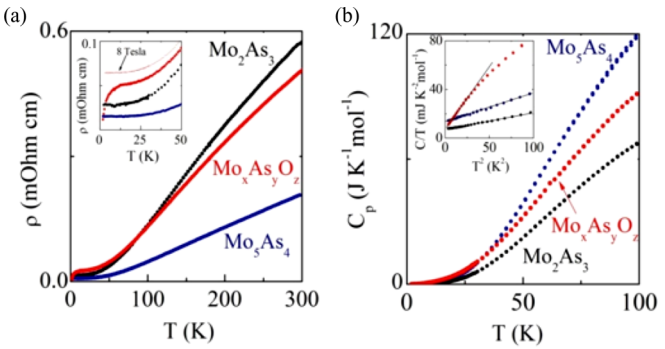

FIG. 4. (Color online) For Mo_2As_3, Mo_5As_4, and $Mo_xAs_yO_z$, temperature dependence of (a) resistivity $\rho(T)$ and (b) heat capacity $C(T)$. Inset of (a) demonstrated the effect of 8 Tesla field on $Mo_xAs_yO_z$. Inset of (b) is the C/T versus T^2 plot at low temperature, with the linear fits.

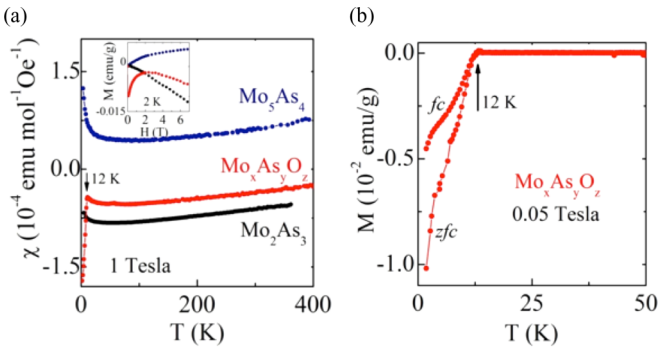

FIG. 5. (Color online) Temperature dependence of (a) zfc magnetic susceptibility for Mo_2As_3, Mo_5As_4, and $Mo_xAs_yO_z$ at applied field of 1 Tesla, (b) zfc and fc magnetization for $Mo_xAs_yO_z$ at the smaller field of 0.05 Tesla. Inset of (a) gives the field dependence of the materials up to 7 Tesla, at 2 K.

used. Mo_5As_4 shows Pauli paramagnetic behavior at $\sim 5 \times 10^{-5}$ emu mol^{-1} Oe^{-1}, having a small upturn in susceptibility below 10 K that could be due to small amount of amorphous paramagnetic impurity. Figure 5(a) inset gives the negative linear dependence of $M(H)$ for Mo_2As_3, positive $M(H)$ dependence for Mo_5As_4 with a small curvature at lower fields. For $Mo_xAs_yO_z$, magnetization, at lower applied field of 0.05 Tesla is shown in Fig. 5(b). There is a clear divergence below $\sim$12 K to negative magnetic susceptibility values, between the zfc and fc forms, which is a sign of shielding and Meissner effects, respectively, in a superconducting sample. Estimation of the superconducting volume fraction based on magnetization measurement shown here gives $\sim$8%, which explains why resistivity does not drop to zero [Fig. 4(a)]. Figure 5(a) inset shows $M(H)$ for this sample, for comparison with pure phases. For $Mo_xAs_yO_z$, magnetization deviates from linear behavior above 900 Oe, suggesting that the lower critical field H_{c1} is approximately 900 Oe

IV. THEORETICAL RESULTS—DENSITY-FUNCTIONAL THEORY CALCULATIONS

First-principles DFT calculations on Mo_2As_3, Mo_5As_4, and MoO_2 were done within the generalized gradient approximation (GGA) [14] using the augmented plane-wave (APW) method [15]. For each of the three compounds, we used approximately 1000 k points in the full Brillouin zone, with sphere radii (in Bohr = 0.529177 Å) for the arsenides of 2.48–2.5 bohr for Mo and 2.20–2.22 bohr for As, while in the oxide the Mo sphere radius was 1.75 Bohr and the O was 1.58 Bohr. An RK_{max} value of 7.0, where R is the minimum sphere radius and K_{max} is the maximum basis set wave vector, was used. No optimization of lattice or internal coordinates was performed; the structural data of Fig. 1 was used. Ionic positions (rounded to three decimal places) were as follows: for Mo_2As_3, the two distinct Mo sites were the 4i sites (0.248,0.371,0.264) and (0.351,0.135, 0.274), while the three distinct As 4i sites were (0.127,0.048,0.384), (0.415,0.685,0.346), and (0.104,0.628,0.324). For Mo_5As_4, the Mo 2a site was (0,0,0), the Mo 8h site (0.300,0.375,0), and the As 8h site (0.051,0.286,0), while for MoO_2 the Mo 4e site was (0.228,0.994,0.013) and the two O 4e sites (0.120,0.230,0.275) and (0.398, 0.685, 0.292).

In Figs. 6(a) and 6(b) we present the Mo_2As_3 and Mo_5As_4 densities-of-states (DOS) calculated from the converged charge density results attained above. The plots also depict the total densities-of-states within each of the muffin-tin spheres. Brillouin-zone integrations for these plots were

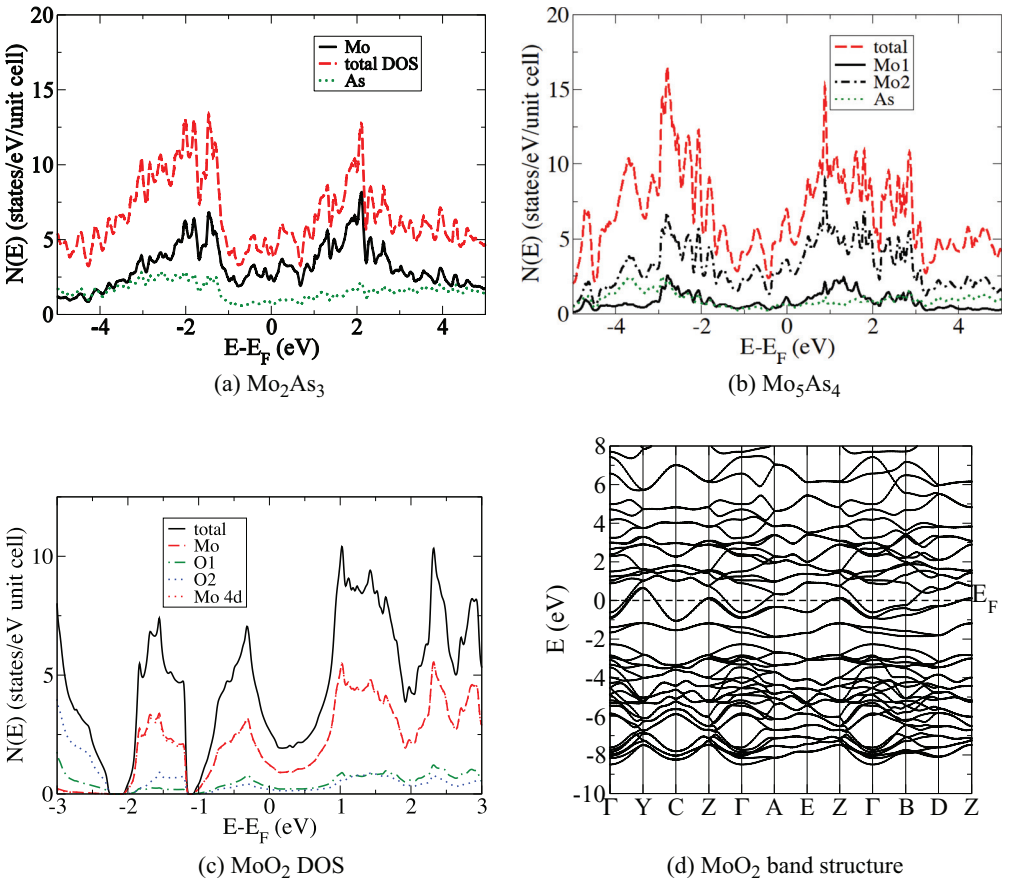

FIG. 6. (Color online) DOS calculation for (a) Mo_2As_3, (b) Mo_5As_4, and (c) MoO_2. For MoO_2 we have plotted both the Mo character and the Mo 4d character, which are virtually identical. Note that for Mo_5As_4 there is one formula unit per unit cell, and for Mo_2As_3 and MoO_2 there are four. For Mo_5As_4, Mo site 1 [the 2a site at (0,0,0)] is of single multiplicity and site 2 is of 4 multiplicity. (d) Calculated band structure of MoO_2 in the simple monoclinic Brillouin zone (note that by convention we have taken the z axis parallel to the original b axis as the other two axes are very nearly the same length.)

carried out using the tetrahedron method. Only nonmagnetic calculations were performed for these compounds. We observe immediately the metallic nature of both compounds, as observed in the experimental resistivities. In addition, in both compounds we note the presence of a gaplike feature around E_F, with a substantial depression in the DOS. For Mo_2As_3 this feature extends some 2 eV above E_F and 1.5 eV below E_F, while in Mo_5As_4 the corresponding range is -3 to $+1$ eV. The widths of the gaplike feature, as well as its depth, are roughly equal in the two compounds (note that the unit cells for these compounds are nearly the same size), with the gap somewhat shifted down in energy, relative to E_F, in Mo_5As_4. The states around E_F for both compounds are primarily of Mo character, and the shape of the Mo-projected DOS is similar to the total DOS, suggesting the dominance of Mo in determining the electronic structure of this material. With the exception of the gap feature shift, the electronic structure of the two systems is quite similar. It remains an open question why the experimental T-linear specific heat coefficient enhancement (relative to the theoretically calculated value) is larger for Mo_2As_3.

The DOS is more complicated for MoO_2 [Fig. 6(c)]. MoO_2 is metallic, similar to Mo_2As_3 and Mo_5As_4 and also exhibits a gaplike feature in the vicinity of the Fermi level. Unlike in the arsenide compound, however, the Fermi level sits directly at one edge of the gaplike feature, with the DOS rising rapidly just below E_F. Due to this highly variable DOS, we have checked for evidence of a hole-doping induced magnetic instability. We note that evidence of magnetism, arising apparently from the presence of oxygen or Mo vacancies, was found experimentally in Ref. [16] and theoretically in Ref. [17]. There is some controversy in the theoretical results, however, as in Ref. [18] no evidence was found for vacancy-related magnetism, but rather for surface-effect magnetism (note that Ref. [16] was a thin-film experiment). We find a Fermi level DOS of 2.68/unit cell eV, which compares fairly well to the previously calculated value [19] of 2.32/u.c. eV. In general the calculated DOS compares reasonably well to that of this earlier reference.

We also depict the calculated nonmagnetic band structure of MoO_2 in Fig. 6(d). We have chosen the same coordinate system and k-point path as Ref. [19] to facilitate comparison with that work. One observes hole pockets around Y and Z as well as an electron surface around G and including B. Three distinct bands cross E_F, and we also observe on the farthest left G-Y panel that these electron and hole pockets are very nearly degenerate, with a rather narrow space between. This will appear in the Fermi surface plots (presented in Fig. 7) and will be seen also to make a contribution to the bare susceptibility as a nesting-type feature. As with the DOS, these results compare fairly well to the earlier results, with some significant differences (such as the presence of an electron pocket around B, not visible in Fig. 6 of Ref. [19].

By studying doping using the virtual crystal approximation, as well as calculations with one of the four equivalent Mo sites substituted with Nb or Zr, we have searched for doping-induced ferromagnetic ground states and find no such state. Indeed, from the DOS plot in Fig. 6(c), one finds that the Stoner criterion for magnetism is not near to being satisfied at any likely hole doping level, as the Mo DOS never exceeds 1 per eV per Mo (both spins), and with the Stoner I of 0.022 Ryd from Ref. [20] one finds a Stoner parameter of less than 0.3. Our results are consistent with the previous theoretical results as regards the lack of magnetism in the pure MoO_2 compound. As many oxides exhibit antiferromagnetism, we have also investigated a nearest-neighbor antiferromagnetic configuration and find that the calculation converges to a nonmagnetic state.

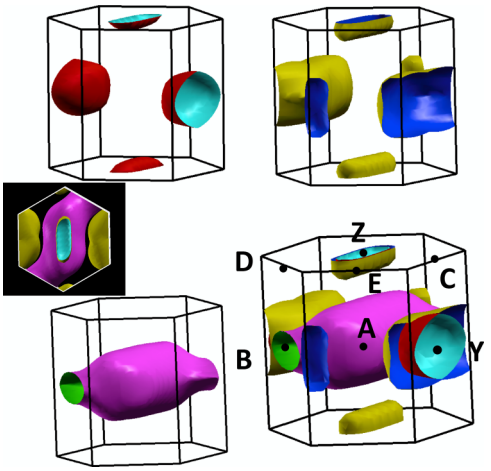

FIG. 7. (Color online) The calculated Fermi surface of nonmagnetic MoO_2. Top left: Band 51 surface (holelike); top right: band 52 surface (holelike); bottom left, band 53 surface (electronlike); bottom right, combined plot. Middle left: A top view of the combined surface; note the parallel band 52 surfaces.

These findings have implications for the superconductivity observed in this material. In some theories superconductivity can arise from a nearly magnetic itinerant ground state. However, most typically this is in competition with an antiferromagnetic state, as observed in the iron pnictides and cuprates, while Ref. [16] found experimental evidence for room-temperature ferromagnetism. While ferromagnetic fluctuations can induce superconductivity or superfluidity, as in ^{3}He [21], this is generally associated with a triplet state which has almost universally a low T_c, certainly not $\sim$12 K. Hence the superconductivity in this material does not appear to derive from the experimentally observed ferromagnetism. There is one other possibility, however, superconductivity deriving from antiferromagnetic *fluctuations*, as opposed to ordering. For this possibility the Fermi surface structure is of interest. Figure 8 depicts the Fermi surface of MoO_2 calculated from the band structure results.

The plots display a complex Fermi surface structure; as mentioned previously, three bands (bands 51, 52, and 53) cross the Fermi energy, depicted, respectively, in the upper left, upper right, and lower left of Fig. 8. Band 51 displays hole pockets around Y and Z, with the former somewhat more anisotropic than the latter. Band 52 contains hole pockets in these same locations, with somewhat different shapes, with an additional pocket located at a point between A and B. Band 53 contains a large electron "tube," centered at Γ and continuing on to the B point. The inset plot above the plot of band 53 depicts all three bands from a top view. Of note are the parallel vertical surfaces in this plot, which could lead to nesting. These results differ somewhat from the Fermi

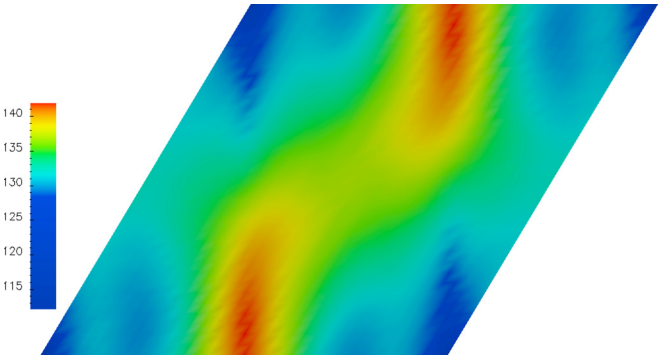

FIG. 8. (Color online) The real part of the Lindhard spin susceptibility calculated in the basal plane for MoO_2. The Γ point is at each of the four corners.

surface plots presented in Ref. [19] as those results pertain to a hypothetical rutile-type tetragonal structure while we have used the actual, experimentally observed monoclinic structure here.

One recalls the situation in the iron pnictides, wherein superconductivity appears to be a result of SDW fluctuations remaining after the doping-induced destruction of the magnetic state. In the present situation the SDW magnetic fluctuations could potentially be sufficiently strong to support superconductivity, but not an itinerant magnetic state, which unlike superconductivity requires minimum interaction (the Stoner criterion) strength, in order to exist.

To examine these possibilities we have computed the real part of the bare Lindhard spin susceptibility $\chi_0(\boldsymbol{q})$ [22,23], which would control the strength of the magnetic-fluctuation-related pairing interaction, if present in MoO_2. Recall that this quantity is generally enhanced by "nesting" Fermi surface features, although not a direct measurement of the nesting. It is defined as follows:

$$Xo(\boldsymbol{q}) = \sum_{\boldsymbol{k},i,j} \frac{f[E(\boldsymbol{k}+\boldsymbol{q},i)] - f[E(\boldsymbol{k},j)]}{E(\boldsymbol{k},j) - E(\boldsymbol{k}+\boldsymbol{q},i) + i\delta}.$$

In this expression f is the Fermi function $\{\exp[(E-\mu)/kT]+1\}^{-1}$, $E(\boldsymbol{k},i)$ is the energy of band number i at wave vector $\boldsymbol{k}$, and the sum is taken over all wave vectors and combinations of bands, including when $i=j$. Here δ is a positive infinitesimal.

In general, within canonical spin-density wave theory, an instability occurs when the RPA susceptibility, defined as

$$X(\boldsymbol{q}) = \frac{Xo(\boldsymbol{q})}{1 - V(\boldsymbol{q})Xo(\boldsymbol{q})}$$

diverges. Here $V(\boldsymbol{q})$ is the interaction vertex, whose momentum dependence is typically weaker than that of the bare susceptibility. Hence spin-density wave *fluctuations*, as could be responsible for superconductivity in MoO_{2-x}, are generally well described by the bare susceptibility $Xo(\boldsymbol{q})$.

We depict this quantity, plotted in the basal (i.e., $q_z = 0$) plane, in Fig. 8. Values generally diminish away from the basal plane. Of note, there is substantial structure in this quantity, with a maximum observed near (0.5,0.1,0) (here the c axis is taken as the b axis from the structural determination). If the observed superconductivity in MoO_2 is due to a magnetic SDW-related mechanism, it might be possible to observe a superconducting order parameter sign change over the wave vectors associated with Fermi surface nesting. For bulk superconductivity, MoO_2 compositions away from stoichiometry (deficient or doped) will need to be synthesized and characterized.

V. CONCLUSIONS

Experimental data and electronic structures of pure MoO_2, as well as Mo_2As_3 and Mo_5As_4, suggest a possibility that the superconductivity likely due to the $MoO_{2-\delta}$ could originate in nesting-type fluctuations, although we find no evidence for magnetism in the MoO_2 sample. More research work will be required to understand and uncover the bulk superconductivity in these samples.

ACKNOWLEDGMENTS

This work was supported by the Oak Ridge National Laboratory LDRD funding program. A.S. also acknowledges support by the Department of Energy, Office of Basic Energy Sciences, Materials Sciences and Engineering Division. Part of this research was conducted at the Center for Nanophase Materials Sciences User Facility (JCI), which is sponsored at ORNL by the Scientific User Facility Division, office of Basic Energy Sciences, US Department of Energy.

[1] A. S. Sefat and D. J. Singh, Mater. Res. Bull. **36**, 614 (2011).
[2] B. Saparov, J. E. Mitchell, and A. S. Sefat, Supercond. Sci. Technol. **25**, 084016 (2012).
[3] D. Hirai, T. Takayama, D. Hashizume, and H. Takagi, Phys. Rev. B **85**, 140509 (2012).
[4] L. H. Dietrich and W. Jeitschko, J. Solid State Chem. **63**, 377 (1986).
[5] P. Jensen, A. Kjekshus, T. Skansen *et al.* Acta Chem. Scand. **20**, 403 (1966).
[6] P. Jensen and A. Kjekshus, Acta Chem. Scand. **20**, 1309 (1966).
[7] A. A. Bolzan, B. J. Kennedy, and C. J. Howard, Aust. J. Chem. **48**, 1473 (1995).
[8] F. A. Grant, Rev. Mod. Phys. **31**, 646 (1959).
[9] O. Fischer, Appl. Phys. **16**, 1 (1978).
[10] L. M. S. Alves, V. I. Damasceno, C. A. M. dos Santos, A. D. Bortolozo, P. A. Suzuki, H. J. Izario Filho, A. J. S. Machado, and Z. Fisk, Phys. Rev. B **81**, 174532 (2010).
[11] L. M. S. Alves, C. A. M. dos Santos, S. S. Benaion, A. J. S. Machado, B. S. de Lima, J. J. Neumeier, M. D. R. Marques, J. Albino Aguiar, R. J. O. Mossanek, and M. Abbate, J. Appl. Phys. **112**, 073923 (2012).

[12] O. L. Krivanek,, G. J. Corbin, N. Dellby, B. F. Elston, R. J. Keyse, M. F. Murfitt, C. S. Own, Z. S. Szilagyi, and J. W. Woodruff, Ultramicroscopy **108**, 179 (2008).
[13] P. B. Allen, Phys. Rev. B **36**, 2920 (1987).
[14] J. P. Perdew, K. Burke, and M. Ernzerhof, Phys. Rev. Lett. **77**, 3865 (1996).
[15] P. Blaha, K. Schwarz, G. Madsen, D. Kvasnicka, and J. Luitz, *WIEN2k, An Augmented Plane Wave + Local Orbitals Program for Calculating Crystal Properties* (K. Schwarz, Techn. Univ. Wien, Austria) (2001).
[16] P. Thakur, J. C. Cezar, N. B. Brookes, R. J. Choudhary, R. Prakash, D. M. Phase, K. H. Chae, and R. Kumar, Appl. Phys. Lett. **94**, 062501 (2009).
[17] F. Wang, Z. Pang, L. Lin, S. Fang, Y. Dai, and S. Han, Phys. Rev. B **81**, 134407 (2010).
[18] J. Nisar, X. Peng, and R. Ahuja, Phys. Rev. B **81**, 012402 (2010).
[19] V. Eyert, R. Horny, K. Höck, and S. Horn, J. Phys.:Condens. Matt. **12**, 4923 (2000).
[20] J. F. Janak, Phys. Rev. B **16**, 255 (1977).
[21] A. J. Leggett, Rev. Mod. Phys. **47**, 331 (1975).
[22] D. Parker and I. I. Mazin, Phys. Rev. B **83**, 180403(R), (2011).
[23] I. I. Mazin, D. J. Singh, M. D. Johannes, and M. H. Du, Phys. Rev. Lett. **101**, 057003 (2008).